

High-resolution infrared thermography for capturing wildland fire behaviour – RxCADRE 2012

Joseph J. O'Brien^{A,G}, E. Louise Loudermilk^A, Benjamin Hornsby^A,
Andrew T. Hudak^B, Benjamin C. Bright^B, Matthew B. Dickinson^C,
J. Kevin Hiers^D, Casey Teske^E and Roger D. Ottmar^F

^AUSDA Forest Service, Center for Forest Disturbance Science, Southern Research Center,
320 Green Street, Athens, GA 30602, USA.

^BUSDA Forest Service Rocky Mountain Research Station, Forestry Sciences Laboratory,
1221 South Main Street, Moscow, ID 83843, USA.

^CUSDA Forest Service, Northern Research Station, 359 Main Road, Delaware, OH 43015, USA.

^DWildland Fire Center, Eglin Air Force Base, 107 Highway 85 North, Niceville, FL 32578, USA.

^EUniversity of Montana, Fire Center, Room 441, Charles H. Clapp Building, Missoula,
MT 59812, USA.

^FUSDA Forest Service, Pacific Northwest Research Station, Pacific Wildland Fire Sciences
Laboratory, 400 North 34th Street, Suite 201, Seattle, WA 98103, USA.

^GCorresponding author. Email: jjobrien@fs.fed.us

Abstract. Wildland fire radiant energy emission is one of the only measurements of combustion that can be made at wide spatial extents and high temporal and spatial resolutions. Furthermore, spatially and temporally explicit measurements are critical for making inferences about fire effects and useful for examining patterns of fire spread. In this study we describe our methods for capturing and analysing spatially and temporally explicit long-wave infrared (LWIR) imagery from the RxCADRE (Prescribed Fire Combustion and Atmospheric Dynamics Research Experiment) project and examine the usefulness of these data in investigating fire behaviour and effects. We compare LWIR imagery captured at fine and moderate spatial and temporal resolutions (from 1 cm² to 1 m²; and from 0.12 to 1 Hz) using both nadir and oblique measurements. We analyse fine-scale spatial heterogeneity of fire radiant power and energy released in several experimental burns. There was concurrence between the measurements, although the oblique view estimates of fire radiative power were consistently higher than the nadir view estimates. The nadir measurements illustrate the significance of fuel characteristics, particularly type and connectivity, in driving spatial variability at fine scales. The nadir and oblique measurements illustrate the usefulness of the data for describing the location and movement of the fire front at discrete moments in time at these fine and moderate resolutions. Spatially and temporally resolved data from these techniques show promise to effectively link the combustion environment with post-fire processes, remote sensing at larger scales and wildland fire modelling efforts.

Additional keywords: fire radiant energy, fire radiant power, long-wave infrared.

Received 13 September 2014, accepted 30 April 2015, published online 22 June 2015

Introduction

Measuring wildland fire is inherently difficult, especially relative to understanding the ecological effects of fire. For many years, the technology available for measuring wildland fire intensity was limited to qualitative descriptions, visual estimates, point measurements or relative indices of intensity (Kennard *et al.* 2005). This hindered the ability to accurately capture fire in ways that could mechanistically link fire behaviour with fire effects, especially in a spatial manner. Direct measurements of energy transfer are critical for predicting and understanding both first- and second-order fire effects

(Van Wagner 1971; Johnson and Miyanishi 2001; Dickinson and Ryan 2010). Recent advances in technology have made it possible to measure the fire energy environment across time and space using infrared thermography. Long-wave infrared (LWIR) thermography is a well established measurement technique (Maldague 2001; Meléndez *et al.* 2010) that is useful because the long wave portion of the infrared spectrum is most sensitive to radiation emitted by surfaces heated by fire, such as fuels, plants, woodland creatures and soils. Furthermore, the system can have a high spatial and temporal resolution and does not require sensor contact with the object being measured.

Table 1. Details of LWIR camera and data acquisition characteristics in this study

All cameras used a focal-plane array uncooled microbolometer with a resolution of either 320×240 (S60) or 640×480 (SC660, T640) and a spectral range of 7.5–13 μm . The SC660 and T640 cameras have a sensitivity of 0.03°C , whereas the S60 has a sensitivity of 0.06°C . All systems have a spatial resolution of 1.3 mRad and a thermal accuracy of $\pm 2\%$. The height of the nadir-view tripod system provided a 4.8×6.4 m field of view for the SC660 and S60 cameras, and a 2.5×3.3 m field of view for the T640. The table below provides information on long-wave infrared (LWIR) image acquisition and for the 2012 RxCADRE (Prescribed Fire Combustion and Atmospheric Dynamics Research Experiment) burns. All super-highly instrumented plots (SHIPs) in the large burn units were nadir views. Camera movement is defined as follows: 1, light (less than ~ 5 pixels); 2, light to moderate (~ 5 – 10 pixels); 3, moderate to heavy (~ 10 – 30 pixels). Ranges in the camera movement column represent where movement intensity changed during data collection (e.g. 1–2 means that light camera movement becoming moderate). Pixel resolution for oblique imagery represents post-processed georectified data

Plot	Data acquired?	Camera (lens)	Frame rate (Hz)	Camera movement	Pixel resolution
L1G SHIP1	Yes	T-640 (25°)	1	2–3	0.53 cm ²
L1G SHIP2	Yes	S-60 (45°)	1	1	1.99 cm ²
L1G SHIP3	No	SC-660 (45°)	–	–	–
L2G SHIP1	Yes	S-60 (45°)	0.17	1	2.02 cm ²
L2G SHIP2	Yes	T-640 (25°)	1	1	0.53 cm ²
L2G SHIP3	No	SC-660 (45°)	–	–	–
L2F SHIP1	No	T-640 (25°)	–	–	–
L2F SHIP2	Yes	S-60 (45°)	0.12	2–3	2.04 cm ²
L2F SHIP3	Yes	SC-660 (45°)	1	1	1.02 cm ²
S3 Nadir	No	S-60 (45°)	–	–	–
S3 Oblique	Yes	SC-660 (45°)	1	1–2	1 m ²
S4 Nadir	No	S-60 (45°)	–	–	–
S4 Oblique	Yes	SC-660 (45°)	1	1–2	1 m ²
S5 Nadir	Yes	S-60 (45°)	1	2	1.95 cm ²
S5 Oblique	Yes	SC-660 (45°)	1	1–2	1 m ²
S7 Nadir	Yes	S-60 (45°)	0.17	2	2.0 cm ²
S7 Oblique	Yes	SC-660 (45°)	1	2–3	1 m ²
S8 Nadir	Yes	S-60 (45°)	0.13	1	1.97 cm ²
S8 Oblique	Yes	SC-660 (45°)	1	2–3	1 m ²
S9 Nadir	Yes	S-60 (45°)	0.14	2–3	2.01 cm ²
S9 Oblique	Yes	SC-660 (45°)	1	1–2	1 m ²

LWIR thermography is especially useful for fire effects research because the LWIR radiation emitted by an object represents the integrated effect of radiative, convective and conductive heating impinging on the object of interest. The system used in this research is designed to detect LWIR, a portion of the electromagnetic spectrum useful for smoky environments because part of the bandpass is minimally affected by fine particulates, hot gas emissions and infrared absorption by gases (Rogalski and Chrzanowski 2002). The principles, benefits and limitations of LWIR thermography are detailed in Loudermilk *et al.* (2012) and Rogalski and Chrzanowski (2002).

The data recorded by LWIR thermography are spatially explicit, and examining the spatial dependencies or autocorrelation of the fire radiation environment can be useful in many ways. First, the data can provide the location and structure of the fire front at discrete points in time. Second, one can decouple the spatial trends to better understand the underlying mechanisms that either drive fire behaviour (e.g. fuel type and arrangement) or how fire behaviour influences subsequent fire effects (Hiers *et al.* 2009; Loudermilk *et al.* 2009, 2012). These spatial trends can also be used to evaluate fire spread models (e.g. Berjak and Hearne 2002; Achtemeier *et al.* 2012) to determine whether they capture the appropriate scale of variability measured in the field. A spatiotemporal analysis could be performed using simultaneously recorded wind data (e.g. with anemometers; Butler *et al.* 2015) to isolate direct wind effects from other fire behaviour

characteristics that may be useful for uncovering the mechanisms driving wildland fire spread.

In this paper we describe our methods for capturing and analysing spatially and temporally explicit LWIR temperature data developed through the RxCADRE (Prescribed Fire Combustion and Atmospheric Dynamics Research Experiment) project and examine the usefulness of these data in investigating fire behaviour and effects. We compare LWIR data captured at fine (1 – 4 cm²) and moderate (1 m²) resolutions and analyse fine-scale spatial heterogeneity of fire radiant power and energy released in several experimental burns.

Methods

For details on the study site and experimental design, see Ottmar *et al.* (2015a).

LWIR thermography measurements

We used two measurement strategies to capture thermal data at fine (1 – 4 cm²) and moderate (1 m²) resolutions. We used three LWIR thermal imaging systems from FLIR Inc. (Wilsonville, OR): the SC660, S60 and T640. All three cameras were used to acquire the fine-resolution imagery, whereas the moderate-resolution imagery was captured exclusively by the SC660. Camera and associated imagery details can be found in Table 1. The fine-scale measurements were captured from an 8.2-m tall



Fig. 1. (a) Tripod system and (b) boom lift used to collect nadir and oblique long-wave infrared (LWIR) thermographic measurements respectively, of surface wildland fires.

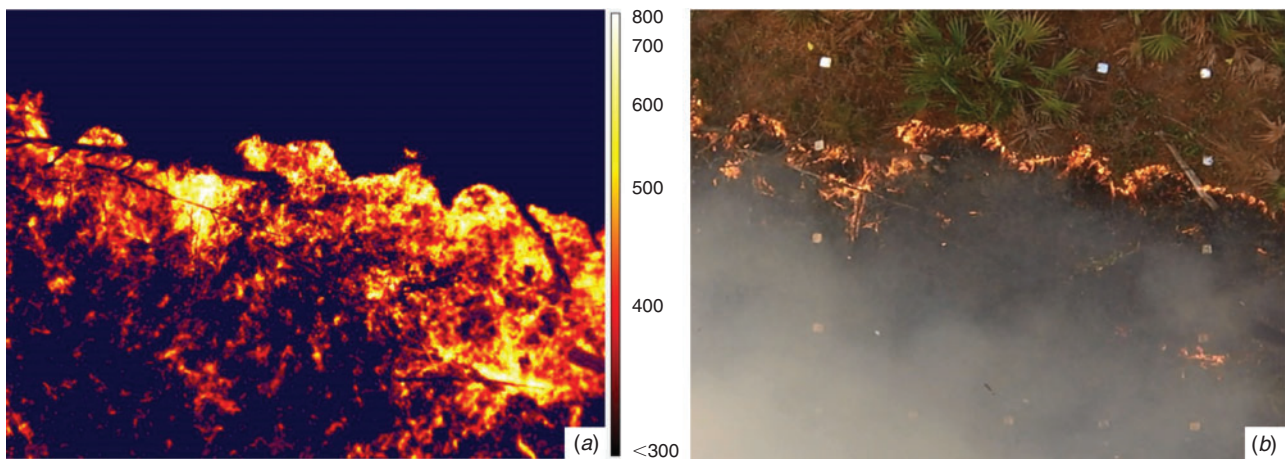


Fig. 2. (a) Snapshot of nadir long-wave infrared (LWIR) imagery versus (b) a colour digital photograph of a surface fire (L2F SHIP 3). Note the transparency of smoke in the LWIR imagery and the detection of thermal signatures of both flaming and smouldering combustion. The metal targets (in *b*) are used for post-processing and are positioned 1-m apart around the perimeter of the super-highly instrumented plot (SHIP). Colour legend for the LWIR image is in $^{\circ}\text{C}$.

tripod (Fig. 1a) designed to provide a nadir perspective, whereas the moderate-scale resolution data were collected at an oblique angle from a 25.9-m boom lift (Fig. 1b). The nadir views were positioned over presurveyed 4×4 m super-highly instrumented plots (SHIPs) located randomly in each 20×20 m highly instrumented plot (HIP; see Ottmar *et al.* 2015a). The SHIPs had 100-cm^2 square steel plates placed at 1-m intervals around the perimeter as ‘cold targets’ (Fig. 2). The low emissivity (ϵ) of the steel made them easily detectable in the thermal image and useful for georeferencing and cropping the SHIPs. The boom lift was located 10–25 m from the control lines demarcating the small units and positioned at the centre of and perpendicular to the ignition line upwind of the units in all cases with the exception of S9. Locating the boom lift upwind lessened the likelihood of unburned fuels obscuring the LWIR signal from

the fire, and being unobscured by smoke provided an additional measure of safety around unmanned aerial systems. For both the nadir and oblique viewing LWIR cameras, an image of the ambient temperature range ($0\text{--}300^{\circ}\text{C}$) was collected just before ignition. These images of ambient conditions were critical for identifying control points for processing.

The tripod system consisted of an equilateral triangular aluminium plate with 1-m sides positioned 8.2 m above the ground by three 3.175-cm diameter American National Standards Institute (ANSI) Schedule 40 pipe legs. The legs consisted of four sections (three aluminium, the lowest steel) connected by ferrules locked in place with D-rings and were attached to each apex of the triangular plate by an axle allowing the legs to swivel in two dimensions. Steel was used for the lowest section because of its high melting point and high density, which increased

tripod stability. The LWIR camera was mounted inside a metal ammunition box with ports cut for optics and cabling that was raised to the bottom of the triangular plate via a 9.5-mm braided steel cable and winch. The LWIR optics were positioned 7.7 m above the centre of the SHIPs. Cabling was armoured by 2.5-cm diameter flexible aluminium conduit.

The SC660 field of view in the oblique imagery covered most of the area of the small burn blocks and captured the entire fire perimeter from ignition until the fire completely passed the central instrument cluster and/or reached the downwind control line. Details on data acquisition are given in Table 1. Emissivity was set at 0.98, the approximate mean of soils and fuels in the wavelengths measured by the FLIR instruments (Snyder *et al.* 1998; López *et al.* 2012), and the air temperature and relative humidity were noted for post-processing. The temperature range for all cameras during the fires was set to 300–1500°C for collecting active fire LWIR data. High-definition digital visual imagery was collected before and during the fire from video cameras located adjacent to the LWIR cameras.

Image processing

The FLIR systems gave radiometric temperatures in °C as raw output. For all LWIR imagery, the native file format was converted to an ASCII array of temperatures in °K with rows and columns representing pixel positions. For the nadir plots (SHIPs), we then extracted the area of interest using code developed in the Python 2.7 (Beaverton, OR) programming language. The selected array of temperatures was converted into another ASCII file of three columns where x, y, z = pixel row, pixel column and temperature. Temperatures were then converted into $W m^{-2}$ (fire radiated flux density; FRFD) using the Stefan–Boltzmann equation for a grey body emitter. Again, ϵ was assumed to be 0.98. We also calculated mean residence time as the average amount of time a pixel was measured to be above the Draper point (525°C) among all pixels in the burn block for the duration of the event and maximum residence time was the maximum number of times a single pixel was measured to be above the Draper point. Our technique likely underestimates the contribution of flames to power and energy release because of low flame ϵ (Johnston *et al.* 2014) and flames whose peak emissions are in the midwave infrared portion of the spectrum, but does accurately capture temperatures of the burning fuel and heated soil. However, these cameras were recently calibrated and we used emissivity values recommended by both the camera manufacturer and for the fuels and soil for the majority of the wavelengths measured by the cameras (Snyder *et al.* 1998; López *et al.* 2012).

For the oblique platform, images were processed using Python 2.7 programming language and rectified using Geospatial Data Abstraction Library (GDAL) v.1.10.1 (Open Source Geospatial Foundation, Beaverton, OR). The image radiometric (effective) temperature values were converted to RGB values in a TIFF file for processing. This entailed converting temperature values into three bands restricted to 256 values. All temperature values were converted to integers. The red band preserved the hundreds and thousands place of the temperature values, whereas the blue band preserved the one to tens place of the temperature values of each temperature value. All green band pixel values were zero (no conversion). The red band pixel

values were calculated using the temperature (T) pixel values in the following equation, with conversions to integer (int):

$$((T/10)_{\text{int}} \times 1.7)_{\text{int}}$$

The blue band was calculated by the following equation:

$$(T_{\text{int}} \times 10 - (T/10)_{\text{int}} \times 100) \times 2$$

Twelve ground control points for each small burn block were identified using surveyed positions of hot targets (e.g. charcoal cans), instruments and ignition points. The pre-fire LWIR image of ambient conditions was critical for identifying ground control points because any surveyed instruments with low ϵ (e.g. tripod, radiometer or any steep instrument enclosures), any obvious ground features (e.g. vegetation or permanent infrastructure) and surveyed hot targets were only visible in this pre-fire image. LWIR images of the initial ignition point and ends of ignition lines, which were surveyed, provided an additional three ground control points. In the end, only the first few images (pre-fire, ignition points) were used for identifying the ground control points. As such, we assumed that the remaining images had the same coordinate frame (i.e. no camera movement). In reality, there was some camera movement, the degree of which was determined by wind conditions. Although this may have intermittently introduced an element of spatial error in the images, the coincidence of the measurements was tested against the nadir images (see below) and showed concordance. Within GDAL, each image was rectified using a third-order polynomial (using the 12 control points), bilinear resampling and the European Petroleum Survey Group (EPSG) projection 26916 (North American Datum (NAD) 83/Universal Transverse Mercator (UTM) zone 16N) with an output resolution of 1×1 m. Once rectified, each image was converted back to radiometric temperature values by back-calculating using the previous equations, and estimates of fire radiative power (FRP) by pixel were calculated using the Stefan–Boltzmann law for a grey body emitter. Fire pixel values were summed across units at each time step to give whole fire total fire radiative energy (FRE; Table 2).

Total fire radiative energy density (FRED) was calculated across oblique LWIR images (Fig. 3). To calculate FRED on a pixel-by-pixel basis, we reduced the geo-registration differences between consecutive images that were caused by camera movement. This was done by resampling images (nearest neighbour) to a common origin and extent using Environment for Visualising Images (ENVI) software (Exelis Inc., McLean, VA). A total FRED image was created using the following:

$$FRED = 10^{-5} \times \sum_{i=2}^n 0.5 \times (FRFD_i + FRFD_{i-1}) \times (t_i - t_{i-1}) \quad (1)$$

where FRED is total fire radiative energy density ($GJ ha^{-1}$), i indicates time step, and t is the measurement frequency (in s; Fig. 3). Image processing was done using the ‘raster’ package (v.2.2–31) in R (R Core Team 2013).

The FRED images (Fig. 3) illustrate the area recorded by the oblique LWIR camera. The camera operation protocol was to

Table 2. Details from oblique long-wave infrared (LWIR) imagery, including fire radiative power estimates

Unless indicated otherwise, data are given as the mean \pm s.d. Oblique LWIR imagery had a resolution of 1×1 m. Total area burned excludes unburned areas (pixels) within burn blocks. FRP, fire radiative power (across pixels); total FRE, total fire radiative energy released from fire recorded in the burn block; total area burned, mean number of 1-m^2 pixels burned at 1 Hz (across LWIR images); FRED, fire radiative energy density (GJ ha^{-1})

Fire	Active flaming duration (min)	Active flaming area (m^2)	Total area burned (ha)	Total FRE (GJ)	FRP (MW)	Maximum FRP (MW)	FRED (GJ ha^{-1})
S3	26	324 ± 286	2.16	5.7	4.2 ± 3.8	15.4	3.0 ± 2.5
S4	20	88 ± 86	0.50	1.3	1.2 ± 1.4	5.5	3.0 ± 2.5
S5	29	289 ± 203	1.14	5.9	3.9 ± 3.0	14.0	3.9 ± 2.9
S7	29	150 ± 217	1.14	3.1	2.1 ± 3.3	18.8	3.0 ± 2.6
S8	23	353 ± 356	2.31	6.3	5.1 ± 6.7	41.7	3.0 ± 3.1
S9	17	177 ± 173	1.82	1.9	2.0 ± 2.0	7.8	1.2 ± 1.0

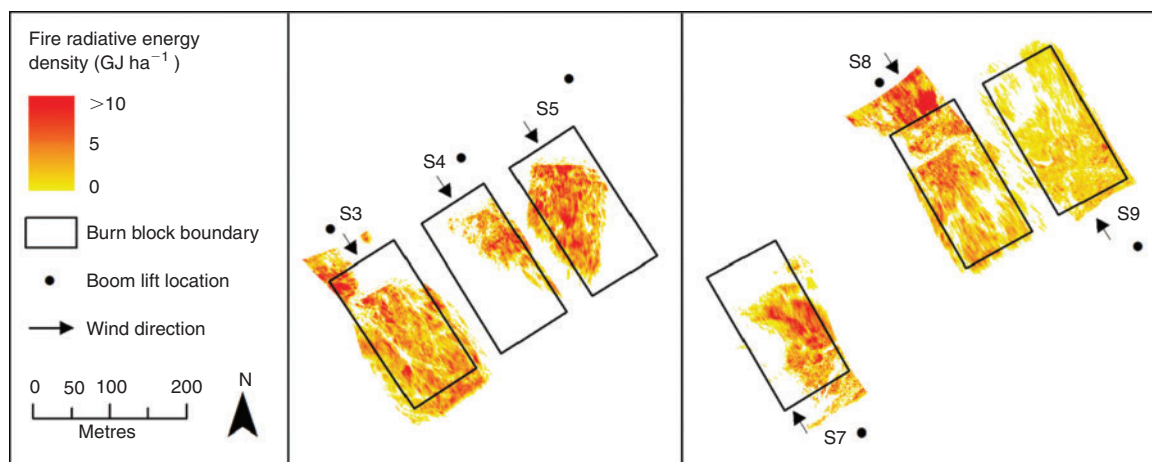


Fig. 3. Total fire radiative energy density (FRED; GJ ha^{-1}) across oblique long-wave infrared (LWIR) imagery. The burn block is a subset of the burn unit or the entire area burned. Indicated wind direction is approximate. Fires were lit outside the unit on the upwind side of the unit and allowed to burn through the burn block and beyond. The boom lift locations indicate where the oblique LWIR camera was positioned 25 m above ground level. The white areas represent where there are no LWIR data, where either that area did not burn or data were not collected because the camera was turned off during that portion of the burn (typically at burn out, towards the end of the burn).

collect imagery until the free running fire passed completely through the HIP or made contact with the downwind fire line at which point the firing operations crew would commence to burn out any remaining unburned fuel within the unit. In S3 and S8 (Fig. 3), we opportunistically captured part of the burnout operation. White areas within the rectangular units in Fig. 3 only reflect that there is no LWIR data and not necessarily where there was no fire. Fig. 3 also illustrates the distortion caused by the oblique angle and camera movement that was not accounted for during the rectification process. This can be seen as the smearing of the temperature data at points farthest from the camera location.

To assess potential measurement error in long-range oblique LWIR measurements, we compared spatially coincident oblique and nadir LWIR estimates of FRP and FRE. Nadir LWIR measurements over a field of view that ranged from 12 to 16 m^2 were made within single 4×4 m SHIPs within each of four small burn blocks (S5, S7, S8, S9; Table 3). The distance between the oblique LWIR camera and the nadir LWIR camera field of view ranged from 125 to 230 m. All inclusive pixels within the 12- to 16- m^2 area (see Table 3) were used for the nadir

LWIR (~ 6400 pixels m^{-2}). Because the oblique LWIR (1 m^2) imagery pixels did not overlap perfectly within the nadir LWIR camera's area, all fully and partially overlapping pixels from the oblique LWIR imagery were used in a bootstrapping technique to estimate a mean and standard deviation of FRP across pixels and images. For example, in each oblique LWIR image in S5 (within the 12- m^2 nadir area field of view; Table 3), 20 overlapping oblique LWIR image pixels were stored as a sample population of LWIR data. We used bootstrapping, sampling 12 pixels with replacement 50 times. From this, we calculated mean \pm s.d. FRP for each image. FRP flux density was the FRP divided by the (12-m^2) area. Total FRE (Table 3) for the oblique imagery is the total 'mean' FRP values from bootstrapping.

Spatial patterns

We chose, as examples, one non-forested (S5) and one forested (L2F HIP3) SHIP to examine the fine-scale spatial heterogeneity of fire behaviour. These plots were chosen for comparison because they had considerable differences in fuel loadings (Ottmar *et al.* 2015b) and overstorey influence (no canopy vs

Table 3. Radiative fire estimates from the nadir and oblique long-wave infrared (LWIR) data within four small (S) non-forested burn blocks and three large (L) burn blocks

Unless indicated otherwise, data are given as the mean \pm s.d. All fire radiative power (FRP) and fire radiative energy (FRE) values from the oblique LWIR data are mean bootstrapped values of overlapping pixels within the nadir LWIR camera's field of view. Total FRE for the oblique LWIR imagery is given as the total mean FRP \pm total s.d. FRP. See Methods for details regarding bootstrapping. There were no usable oblique LWIR data collected at the large burn blocks, and S7 data within the overlap area was corrupted by camera movement. All blocks except L2F were non-forested. FRED, fire radiative energy density

	Block							
	S5		S7		S8		S9	
	Nadir	Oblique	Nadir	Oblique	Nadir	Oblique	Nadir	Oblique
FRP (kW)	33 \pm 32	42 \pm 32	7 \pm 9	–	16 \pm 28	30 \pm 26	34 \pm 47	56 \pm 40
Maximum FRP (kW)	99	103	32	–	85	95	117	109
Mean FRP flux density (kW m ⁻²)	2.8	3.6	0.4	–	1.3	9.5	2.1	4.9
Maximum FRP flux density (kW m ⁻²)	8.3	10.1	2.0	–	7.1	18.7	7.3	6.8
Total FRE (MJ)	3.2	2.1 \pm 0.6	2.2	–	1.2	2.0 \pm 0.6	1.4	1.3 \pm 0.3
Total FRED (MJ m ⁻²)	0.267	0.175 \pm 0.050	0.144	–	0.103	0.17 \pm 0.05	0.107	0.108 \pm 0.025
Total area overlap (m ²)	12	12	16	–	12	12	16	16

	Nadir LWIR plot					
	L1G Plot 1	L1G Plot 2	L2G Plot 1	L2G Plot 2	L2F Plot 2	L2F Plot 3
	FRP (kW)	15 \pm 26	27 \pm 24	23 \pm 29	14 \pm 23	33 \pm 47
Maximum FRP (kW)	84	70	90	83	156	208
Mean FRP flux density (kW m ⁻²)	3.7	2.3	1.4	3.4	2.1	2.6
Maximum FRP flux density (kW m ⁻²)	20.9	5.5	5.6	20.8	9.7	13
Total FRE (MJ)	1.3	3.2	3.2	2.1	12	12.1
Total FRED (MJ m ⁻²)	0.325	0.267	0.2	0.525	0.75	0.756
Total area measured (m ²)	4	12	16	4	16	16

canopy) and were quality, high-sample frequency datasets (collected at 1 Hz). We tested for and modelled the spatial dependencies (autocorrelation) within each of these plots. Moran's I was calculated using the Analyses of Phylogenetics and Evolution ('ape' v.3.0–10) library package in the R programming language v.3.0.1 (R Core Team 2013) to test for spatial autocorrelation. To assess the range of spatial correlation and magnitude of spatial variability of FRE (J) and residence time (s) within these plots, we modelled the semivariance (spatial autocorrelation function) using the geostatistics data analysis (geoR v.1.7–4) and statistical data analysis (StatDA v.1.6.7) library packages in R. An isotropic exponential autocorrelation function (Goovaerts 1997) was fit to the empirical semivariance, with a maximum range of 2 m (\sim 1/2 plot distance). An individual nugget parameter was fit to each model, whereas sill and range parameters were automated within R.

Temporal patterns

Temporal autocorrelation and its confidence interval (CI) were determined for each time series of whole-fire FRP derived from oblique LWIR imagery of small burn blocks. Autocorrelation and 95% CIs were determined using SAS 9.4 PROC TIMESERIES (SAS Institute Inc., Cary, NC, USA). Significant autocorrelation was determined if the autocorrelation for a given lag was less than 1.96 standard deviations from zero (i.e. 95% CI). The longest significant lag is reported.

Results

A comparison of LWIR and visual imagery shows that the LWIR imagery captures a broader range of the combustion

environment (both smouldering and flaming phases), whereas only the flaming phase of combustion was apparent in the visual images (Fig. 2). Both the nadir and oblique (rectified) LWIR imagery illustrated variability in FRP influenced by fuels and changing wind patterns at the flaming front at both fine (Figs 4, 5) and moderate (Fig. 6) scales. These data reflect the heterogeneity of FRP that was released from these surface fires at both fine and coarse scales. This was shown in the nadir LWIR imagery (e.g. Fig. 2a), where detailed fire line intensity was highly variable within a small area (\sim 16 m²). This also was evident in the oblique LWIR imagery (Fig. 7), where fire line geometry and shifting wind patterns influenced fire line depth (e.g. backing vs flanking fire) and total FRED across the burn block (Fig. 3). Because the fire line depth was often within 2 m, the nadir LWIR camera was able to record FRP of the true flaming front, without the signal attenuation that may be caused by blending burning and non-burning areas within pixels at coarser scales. The smooth rise and fall of the FRP at fine scales seen in the non-forested compared with forested SHIPs are not likely an artefact of sampling rate because S5 imagery was collected at 1 Hz compared with all others being collected at approximately 0.15 Hz. This smoothness of FRP in the non-forested SHIPs (Figs 4, 5) is more likely because of the simpler fuel bed of grasses and forbs. The forested SHIPs (Fig. 5) had more heterogeneous fuels, including woody debris, larger patches of shrubs and pine needle litter, causing more temporal variability in FRP (but see spatial heterogeneity of FRE in the Spatial and Temporal Patterns section below).

In the oblique LWIR imagery, total FRE ranged from 1.3 to 5.9 GJ within 0.5–2.31 ha burned within the six small

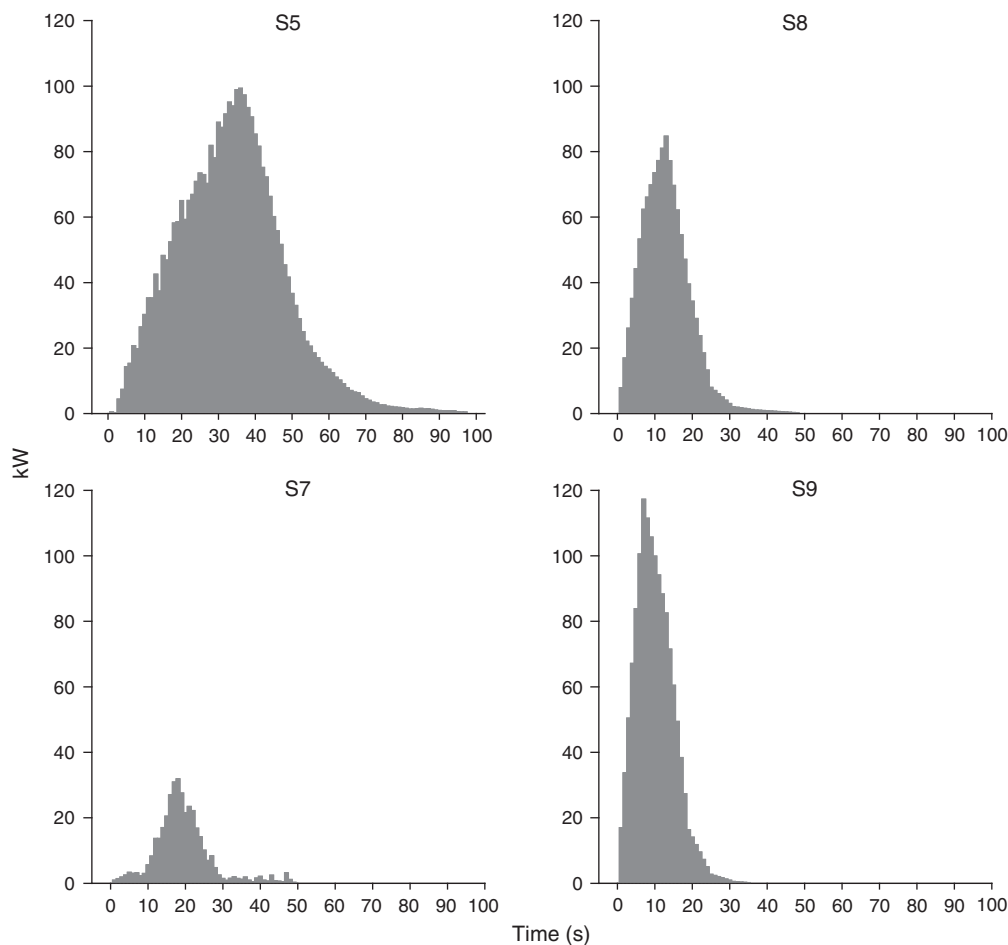


Fig. 4. Nadir long-wave infrared (LWIR) fire radiative power (FRP) measurements within 4×4 m super-highly instrumented plots (SHIPs) in four of the small burn blocks. Data from S3 and S4 are missing because of failure of the camera to acquire imagery.

non-forested units (Table 2). Mean FRED ranged from 1.2 to 3.9 GJ ha^{-1} . Mean and maximum FRP ranged from 1.2 to 5.1 MW and from 5.5 to 41.7 MW respectively. The mean active flaming area (number of pixels) across images ranged from 88 to 353 m^2 , with considerable variation within each fire (s.d. $86\text{--}356 \text{ m}^2$). In the nadir LWIR imagery, total FRE ranged from 1.2 to 12.1 MJ, within a $4\text{--}16 \text{ m}^2$ plot area in the 10 SHIPs (Table 3). Mean and maximum FRP ranged from 14 to 41 kW and from 70 to 208 kW respectively. Mean and maximum FRP flux density ranged from 1.3 to 3.7 and from 5.5 to 20.9 kW m^{-2} respectively. Mean and maximum FRP, as well as mean FRP flux density, between the oblique and nadir LWIR imagery were similar (Figs 8, 9; Table 3), but consistently higher in the oblique LWIR estimates across plots (except for maximum FRP flux density in S9) although we were unable to test the significance of this difference because of a lack of replication. We were unable to compare between the oblique and nadir LWIR data in S7 because we could not ensure proper spatial overlap of the two instruments. The comparison of maximum power among the techniques may be misleading because of the high-frequency fluctuations of peak fire power that are underestimated when sampling at frequencies less than approximately 100 Hz,

although integrated measurements are less affected even with sampling frequencies of 1 Hz (Frankman *et al.* 2013). Total FRE from the oblique LWIR data was comparable to the nadir LWIR data, but had mixed results (Table 3). For instance, the oblique FRE estimates were lower for S5 (2.1 (s.d. 0.6) vs 3.2 MJ), higher for S8 (2.0 (s.d. 0.6) vs 1.2 MJ) and very similar for S9 (1.3 (s.d. 0.3) vs 1.4 MJ) compared with nadir estimates.

Spatial and temporal pattern

The comparison between the two SHIPs, L2F HIP 3 (forested) and S5 (non-forested), exhibited heterogeneity in FRE (Fig. 10), although the scales differed in both space and time. Fig. 10 shows the spatial pattern of FRE found within and between these SHIPs that can be measured using LWIR cameras. Although the total FRE in the forested SHIP (12.1 MJ) was approximately fourfold higher than in the non-forested SHIP (3.2 MJ), the spatial heterogeneity was lower (Fig. 11). Fig. 11 illustrates how the spatial variability can be modelled statistically using semi-variograms within these same SHIPs. Both SHIPs illustrated significant ($P < 0.05$) positive spatial autocorrelation of FRE and residence time, and the range (distance) of spatial variability

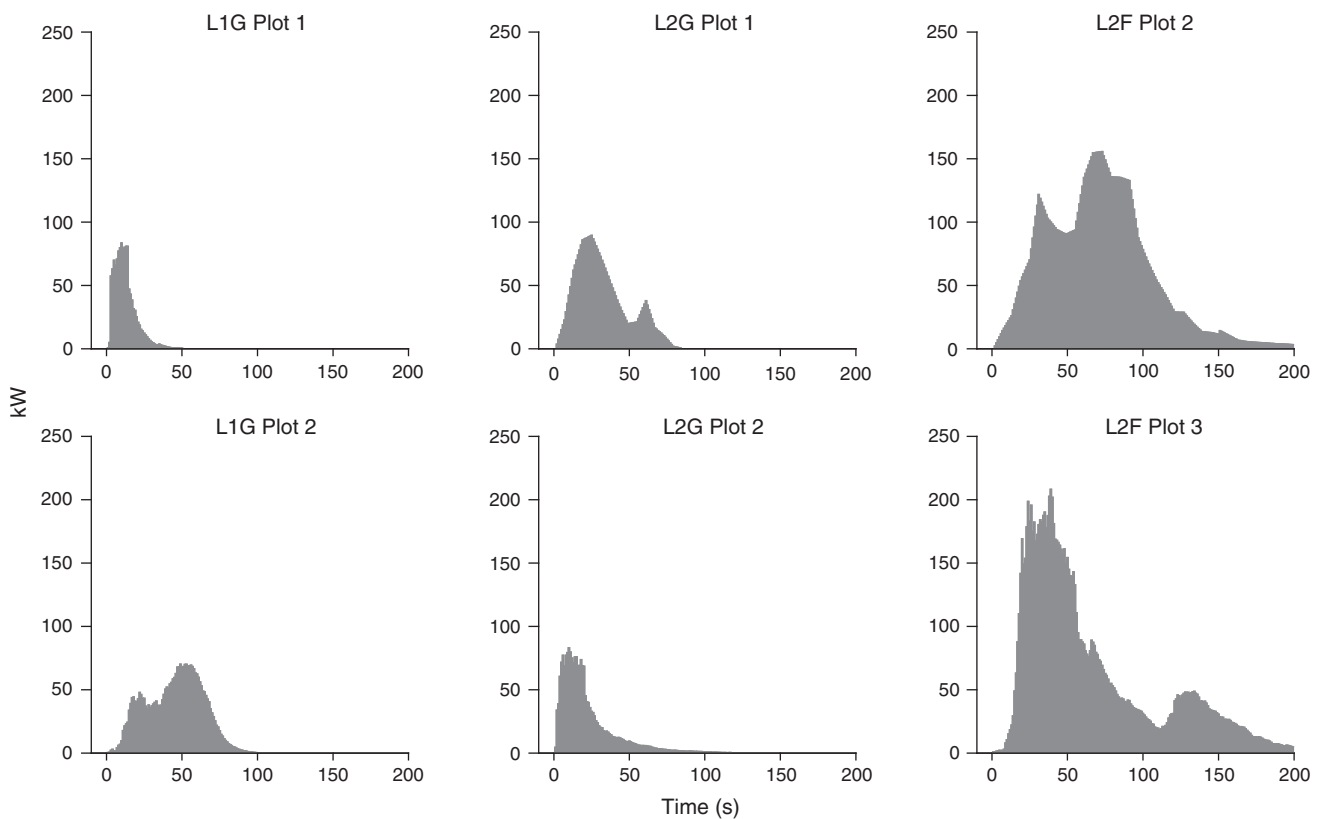


Fig. 5. Nadir long-wave infrared (LWIR) fire radiative power (FRP) measurements within 4×4 m super-highly instrumented plots (SHIPs) in the large burn units. SHIPs labelled L1G and L2G were not forested, whereas SHIP L2F was forested. Note the longer residence time and greater FRP in the forested SHIPs.

among SHIPs was within 1 m. The difference between SHIPs was noted by the magnitude of spatial variability (i.e. partial sill) between SHIPs (Fig. 11). Mean (\pm s.d.) residence time was 20 ± 16 and 44 ± 44 s for the non-forested and forested SHIPs respectively. Maximum residence time was 96 and 672 s for the non-forested and forested SHIPs respectively.

The time series analysis showed that whole-fire FRP for small burn blocks ($n = 6$) was significantly autocorrelated with an average of 1.2 min. The range in longest significant lag was 0.9–1.6 min and the s.d. was 0.4 min.

Discussion

Precise measurements at multiple scales in space and time were key for capturing and understanding the variability associated with our experimental fires. We observed the expected variation in FRE and FRP between different fuel types (forested vs non-forested units), but also detected a large amount of variation within fuel types. This variation was evident over multiple scales, despite the relatively homogeneous vegetation of managed grassy fields and prescribed fires lit under similar conditions. For example, from the oblique LWIR imagery in the six small burn blocks, mean FRP ranged from 1.2 to 5.1 MW and the maximum FRP ranged from 5.5 to 41.7 MW, whereas mean FRED ranged between 1.2 and 3.9 GJ ha⁻¹ across burn blocks (Fig. 3).

Our techniques for using LWIR thermal imagers allowed us to collect precise fine ($1\text{--}4\text{ cm}^2$) and moderate (1 m^2) resolution fire behaviour from both nadir and oblique angles. We found a promising coincidence of measurements of FRP and total FRE between the two instruments from the two perspectives. The rectification process generated comparable FRP and total FRE between oblique- and nadir-viewing LWIR cameras (Table 3; Figs 8, 9). These data and relationships across scales are just beginning to be explored quantitatively. Although the nadir LWIR imagery has been quantified and analysed previously for surface fires (Hiers *et al.* 2009; Loudermilk *et al.* 2012), the oblique LWIR data were novel. Here, we were able to exploit LWIR data across a 2-ha area to provide georeferenced FRFD of a moving surface fire at 1 Hz over the entire fire perimeter throughout the 20–30 min prescribed burns (e.g. Fig. 7).

Although total FRE from the oblique LWIR imagery was variable (see Table 3) when compared with the nadir imagery within the 12–16 m² areas of coincidence (e.g. Fig. 8c), the results were similar even given the difference in spatial resolution between the instruments (1 m^2 vs $\sim 4\text{ cm}^2$). We could not definitively identify the cause of the discrepancies between the measurements, but we can infer that camera movement, absorption of radiant energy by intervening atmosphere, pixel distortion caused by the rectification process and the distance of the SHIP from the oblique instrument platform were likely responsible for the differences we observed. For example, the total

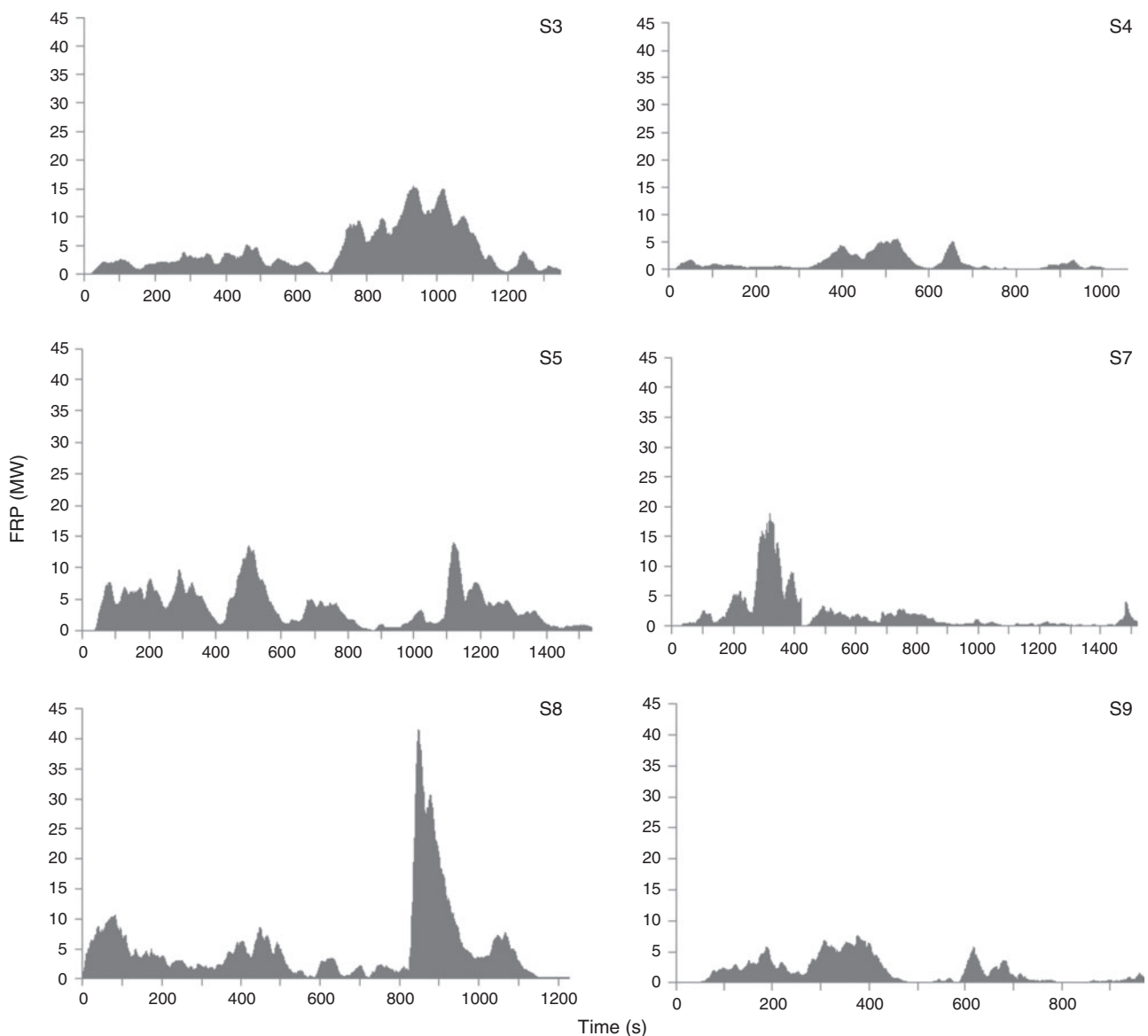


Fig. 6. Temporal fire radiative power (FRP; MW) at 1 Hz collected across the entire small non-forested burn blocks using the oblique long-wave infrared (LWIR) imagery. Fluctuations in FRP are in response to changes in fuels wind patterns and velocity, as well as fire line depth and extent within each block. Time relates to the amount of time between ignition and the fire leaving the camera's field of view and/or reaching the downwind control line. Note the difference in scale of FRP and time between graphs. Graphs are labelled by block names.

FRE of the oblique LWIR imagery was higher than the nadir for S8 (2.0 (s.d. 0.6) vs 1.2 MJ) likely because of the camera movement we saw in the video sequences. This would result in commission errors from pixels outside the nadir plot. In another instance, total FRE was lower in S5 for the oblique data (2.1 (s.d. 0.6) vs 3.2 MJ), likely due to signal attenuation narrowing the power distribution curve (Fig. 8a). Total FRE was most comparable for S9 (oblique vs nadir: 1.3 (s.d. 0.3) vs 1.4 MJ), where the entire curve of FRP was captured by both instruments (Fig. 9b) because the nadir plot was comparatively stable and closer to the oblique view platform (125 m for S9 vs 190 m for S5 and 230 m for S8). Nevertheless, because the oblique LWIR imagery was collected at lower angles and

greater distances (125–230 m) than the nadir LWIR imagery, these measurements were more susceptible to the aforementioned errors. Because the nadir camera was securely positioned directly above the fire and less than 8 m from the ground, errors of distortion or omission and commission were minimal.

Signal attenuation in the oblique views was likely an important source of error because pixels included both burning and non-burning areas that would tend to reduce the average radiometric temperature and, given the fourth-power dependency between temperature and FRFD through the Stefan–Boltzmann equation, attenuate the signal emanating from the fire line. From this, we concluded that if the imager has a minimum resolution greater than the maximum fire line depth, FRP within pixels can

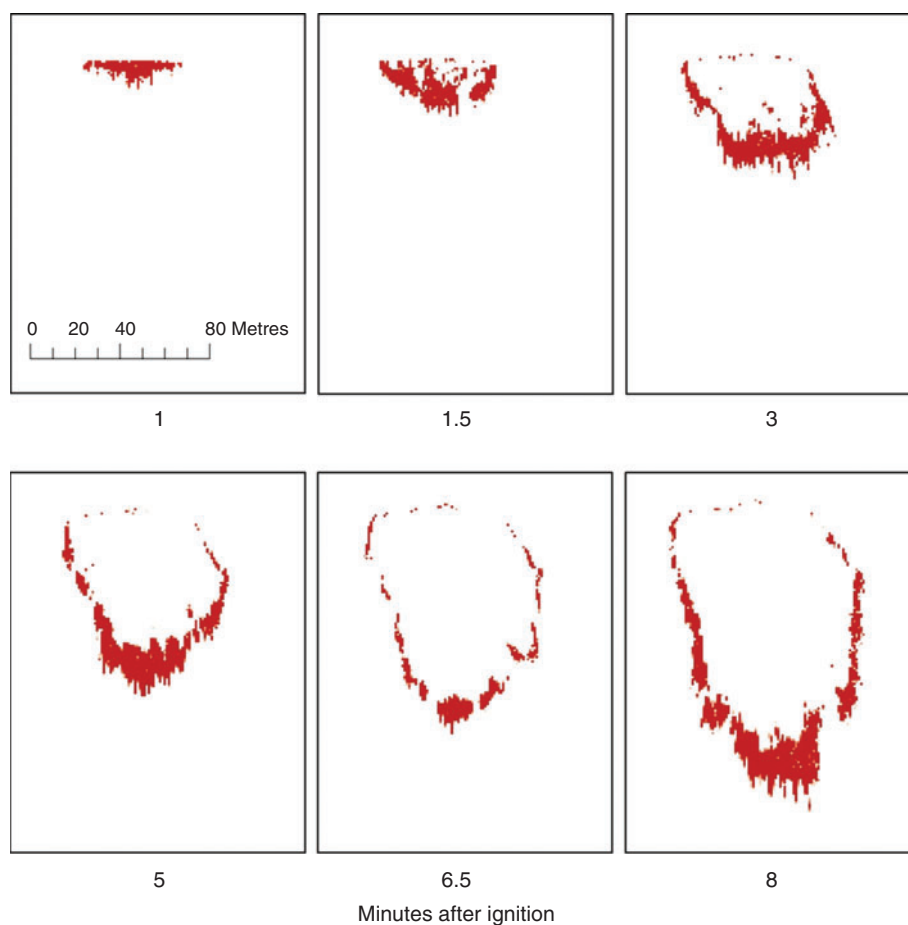


Fig. 7. Chosen oblique long-wave infrared (LWIR) images of a small burn block (S5) representing the moving fire front. At 1 min, the fire is still moving along the original ignition line. By 3 min, the fire develops flanks. Differences in the width of the flaming front illustrate changes in wind velocity and direction. Image resolution 1×1 m. Approximate area in figure display: 2 ha (100×200 m).

be underestimated, a common issue with more coarse scale remote sensing of FRP. For example, in S5, the nadir LWIR images (data not shown, but see Fig. 2 for example) illustrate that the fire line depth was less than 2 m. The 1-m^2 pixels of the oblique LWIR imagery integrated radiation from both burning and non-burning areas, which created opportunities for errors of omission as the fire entered and left the SHIP area (see tails of distribution of FRP, Fig. 8a, b). Even with these discrepancies, the similarities in FRE slopes (Fig. 8c) between the two LWIR systems illustrated that overall fire behaviour dynamics were captured by the oblique LWIR imagery. Furthermore, the oblique LWIR image overlay of the total area sampled (Fig. 3) allows for cross-platform comparisons (e.g. Hudak *et al.* 2015; Dickinson *et al.* 2015) and provides opportunities for further analysis with spatial fuels (from terrestrial Light Detection and Ranging (LIDAR); e.g. Loudermilk *et al.* 2009; Rowell *et al.* 2015) and influential weather characteristics, such as wind patterns from anemometers (Butler *et al.* 2015).

The oblique platform was not effective in the large forested unit of this study, primarily because of canopy obstructing the view of the surface fire. Using the oblique approach would be

most effective when deployed under a tree canopy or in shrublands and grasslands. Although the signal obstruction within the non-forested units was not quantified, it was likely minimal because the fuels were of low stature and relatively sparse. The one oblique camera (S9) positioned in front of the moving fire, where obstruction by unburned fuels was most likely still, resulted in similar estimates of FRP and total FRE compared with at nadir (Table 3). To reduce potential radiation obstruction, we recommend positioning the imaging system upwind of head fires that would remove fuels in the optical path of the camera.

Spatial and temporal autocorrelation

The spatial variability of fire behaviour within and among plots can be influenced by many factors, such as fuel loading and type; fuel structure, including fuel continuity; and local weather (wind, ambient temperature and relative humidity). We chose two contrasting SHIPs (one forested, one non-forested) in this study to provide an example of the distinct spatial heterogeneity that can be found at fine scales within and across these surface

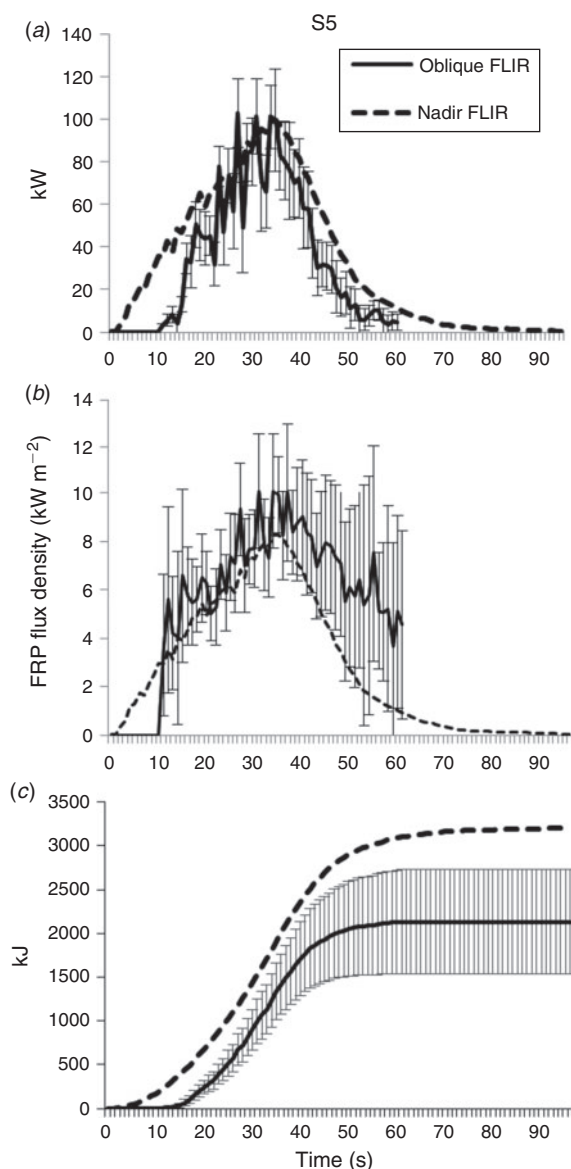


Fig. 8. Cross-scale comparison of fire radiative power measured from the oblique (rectified) and nadir cameras within the same area (the 4×4 m nadir long-wave infrared (LWIR) field of view) within the S5 block. Data are represented as (a) fire radiative power (FRP; kW) at each time stamp, (b) FRP flux density (kW m^{-2}) at each time stamp and (c) cumulative fire radiative energy (FRE) released from fire (kJ). Total (\pm s.d.) FRE released from the fire within the super-highly instrumented plots (SHIPs) was 2.1 ± 0.6 and 3.2 MJ for the oblique and nadir imagery respectively. The x-axis represents relative time from initial fire detection in the 4×4 m SHIPs. FRP for the oblique long-wave infrared (LWIR) is represented as mean and standard deviation of 20 overlapping oblique 1-m^2 pixels within the 12-m^2 SHIPs.

fire regimes. For these two example SHIPs (Figs 10, 11), we found that although the total FRE was almost fourfold greater in the forested than non-forested plot (12.1 vs 3.2 MJ), the spatial variability of FRE was lower in the forested plot (Fig. 11). This is likely due to the connectivity of fuels (pine litter and grasses) within this forested plot compared with the patchiness (bare soil

and grass clumps) in the non-forested plot (Fig. 10). In contrast, the spatial variability of residence time was higher in the forested plot (Fig. 11). This was likely due to smouldering of woody debris found within the forested plot compared with the rapid ignition and consumption of grasses in the non-forested plot. These results relate to previous work where we found that heterogeneity in similar frequent low-intensity fires was driven by fuel type and fuel structure (Loudermilk *et al.* 2012) and less by fuel loadings. Moreover, the abundance of pine litter may be a factor. There was no pine litter in the non-forested plot (Ottmar *et al.* 2015b), reducing both fuel continuity and energy potential (Fonda and Varner 2004).

In future studies, infrared imagery with comparable spatial and temporal resolution and extent will likely be valuable in understanding the relative role of fuels and wind fields on fire radiant emissions and fire spread. For instance, temporal autocorrelation was observed up to 1.2 min on average, which can be related to coincident meteorological measurements. The 1.2-min temporal autocorrelation was likely largely dependent on wind gusts and shifts, although fuel variability may also have played a role (see Rowell and Seielstad 2015).

Considerations for LWIR imagery measurements

There are several considerations that are important when collecting and analysing LWIR thermographic measurements. Camera stability is critical because image georeferencing, cropping and rectification all depend on initial LWIR images (e.g. pre-fire 'cold' image) that were used for locating the ground control points. In our processing approach, all remaining images were assumed to have the same coordinate frame; thus, any camera movement would introduce error in the form of noise or potential bias. Identifying an object in the LWIR requires that it be either warmer or cooler or have a different ϵ than the surroundings. The deployment of targets detectable at the imager temperature scales required for measuring fire would allow frame-by-frame rectification. Unfortunately, very hot targets are difficult to deploy and potentially dangerous. If the imager platform is stable, the difficulties associated with hot targets can be mitigated by using markers made of low ϵ materials. These materials with an $\epsilon < 0.3$ appear markedly colder than the surrounding high ϵ soil and vegetation. These cold targets worked especially well for the nadir measurements. Hot targets (e.g. charcoal canisters) were especially effective for the oblique rectification process because they were more apparent at greater distances, although low ϵ instrument enclosures and other permanent structures were also useful as control points. In images with active fire, control points were difficult to see and were often invisible (Fig. 2a). As such, the pre-fire image of ambient conditions was critical for identifying the control points.

Conclusions

LWIR imagery at multiple scales offers an opportunity to effectively link the combustion environment with post-fire processes, remote sensing at larger scales and wildland fire modelling efforts. Precise measurements at multiple scales in space and time were key for capturing and understanding the

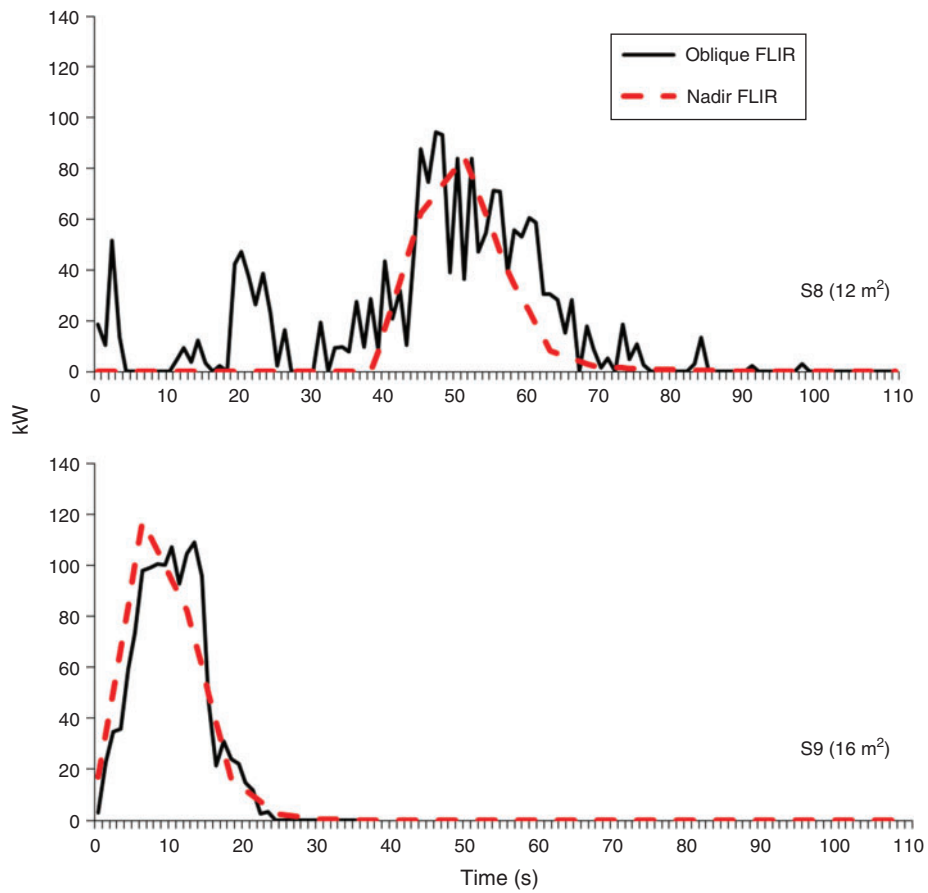


Fig. 9. Nadir and oblique imagery comparison of fire radiative power (FRP) in small burn blocks S8 and S9. Nadir and oblique data were collected at approximately 1 and 0.17 Hz for S8 and S9 respectively. Data correspond to an overlap in area of 12 m² and 16 m² for S8 and S9 (b) respectively. Note the early fluctuations in FRP in S8, where camera movement on the oblique platform caused temporal and spatial shifts in data collection (increased omission and commission errors) compared with S9, where there was little camera movement. Start time (0) is when the fire is first detected by either the oblique or nadir long-wave infrared (LWIR) camera within each respective boundary area.

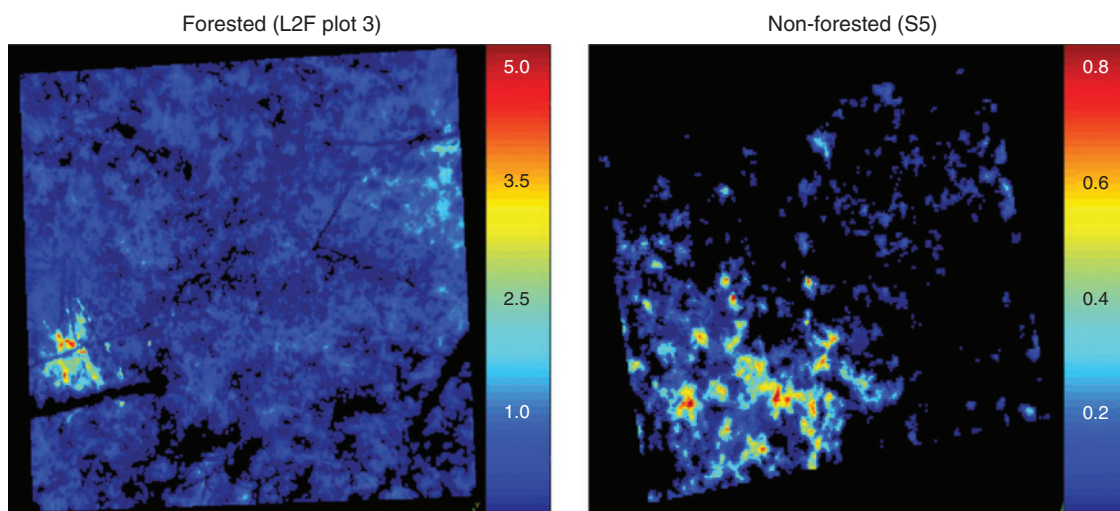


Fig. 10. Example of spatially explicit fire radiative energy (FRE) estimated with the nadir imagery in one forested (L2F SHIP 3) and non-forested super-highly instrumented plot (SHIP; S5). Note the nearly fourfold greater FRE values in the forested SHIP and difference in patchiness of FRE density (FRED) between SHIPs. The scale bar is in FRED (J m⁻²).

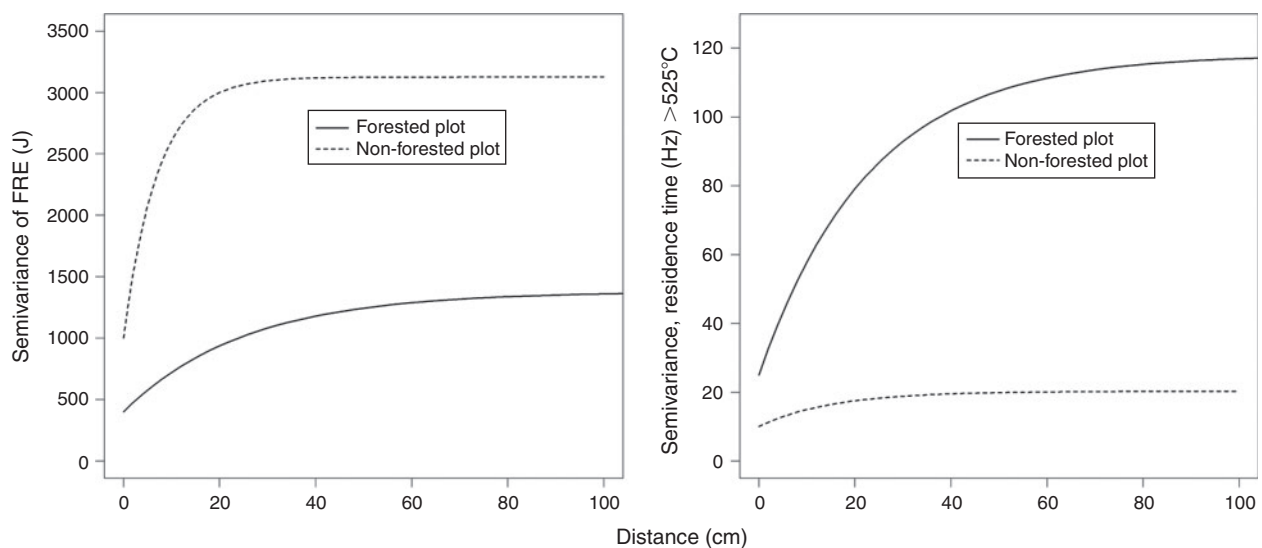


Fig. 11. Modelled spatial autocorrelation of fire radiative energy (FRE) and residence time within one non-forested (S5) and one forested (L2F HIP3) super-highly instrumented plot (SHIP).

variability associated with our experimental fires. Both the nadir and oblique LWIR data provide the utility for describing the location and movement of the fire front at discrete moments in time. These kinds of data will be critical for the development and evaluation of new fire behaviour models that incorporate both stochastic and mechanistic processes that occur across scales. The accurate two-dimensional spatial measurements of surface radiative energy release over time can connect fire to processes such as soil heating, plant mortality and tissue damage, as well as provide valuable data on fire spread and radiant energy fluxes useful for refining fire spread and smoke dynamics models (e.g. Achtemeier *et al.* 2012; Achtemeier 2013). The present study also supports the potential for fine-scale measurements to mechanistically link fire behaviour and fire effects. For example, in longleaf pine (*Pinus palustris* Mill.) forests, plant–plant interactions that make up the diverse understorey are driven not only by frequent fire (Kirkman *et al.* 2004), but also by fine-scale heterogeneity of fuels that are determined by the tree canopy (Mitchell *et al.* 2006), which, in turn, drives fine-scale fire effects (e.g. Wiggers *et al.* 2013). From the moderate-scale fire behaviour data (oblique LWIR imagery), coarser-scale fire patchiness could be linked to vegetation patterns occurring at similar scales.

Acknowledgements

This research was funded primarily by the Joint Fire Science Program (Project #11-2-1-11) with additional support from the US Department of Defence Strategic Environmental Research and Development Program (#RC-2243). Brett Williams of the Jackson Guard Wildland Fire Center went above and beyond the call of duty as incident commander. The authors thank all the Jackson Guard wildland fire personnel because the success of RxCADRE depended on their skill and professionalism. The authors thank Mac Callahan, Christie Stegall, Dexter Strother and Evelyn Wenk of the USDA Forest Service, who were invaluable in the field. The authors also thank Dr Morgan Varner and Dr Jesse Kreye for both sharing equipment and assisting in the field.

References

- Achtemeier GL (2013) Field validation of a free-agent cellular automata model of fire spread with fire–atmosphere coupling. *International Journal of Wildland Fire* **22**, 148–156. doi:10.1071/WF11055
- Achtemeier GL, Goodrick SA, Liu Y (2012) Modeling multiple-core updraft plume rise for an aerial ignition prescribed burn by coupling Daysmoke with a cellular automata fire model. *Atmosphere (Basel)* **3**, 352–376. doi:10.3390/ATMOS3030352
- Berjak SG, Hearne JW (2002) An improved cellular automaton model for simulating fire in a spatially heterogeneous savanna system. *Ecological Modelling* **148**, 133–151. doi:10.1016/S0304-3800(01)00423-9
- Butler B, Teske C, Jimenez , O'Brien JJ, Sopko P, Wold C, Vosburgh M, Hornsby B, Loudermilk EL (2015) Observations of energy transport and rate of spreads from low-intensity fires in longleaf pine habitat – RxCADRE 2012. *International Journal of Wildland Fire* **25**, 76–98. doi:10.1071/WF14154
- Dickinson MB, Ryan KC (2010) Introduction: strengthening the foundation of wildland fire effects prediction for research and management. *Fire Ecology* **6**, 1–12. doi:10.4996/FIREECOLOGY.0601001
- Dickinson MB, Hudak AT, Zajkowski T, Loudermilk L, Schroeder W, Ellison L, Kremens RL, Holley W, Martinez O, Paxton A, Bright BC, O'Brien JJ, Hornsby B, Ichoku C, Faulring J, Gerace A, Peterson D, Mauceri J (2015) Measuring radiant emissions from entire prescribed fires with ground, airborne and satellite sensors – RxCADRE 2012. *International Journal of Wildland Fire* **25**, 48–61. doi:10.1071/WF15090
- Fonda R, Varner J (2004) Burning characteristics of cones from eight pine species. *Northwest Science* **78**, 322–333.
- Frankman D, Webb BW, Butler BW, Jimenez D, Harrington M (2013) The effect of sampling rate on interpretation of the temporal characteristics of radiative and convective heating in wildland flames. *International Journal of Wildland Fire* **22**, 168–173. doi:10.1071/WF12034
- Goovaerts P (1997) 'Geostatistics for natural resources evaluation.' (Oxford University Press: New York.)
- Hiers JK, O'Brien JJ, Mitchell RJ, Grego JM, Loudermilk EL (2009) The wildland fuel cell concept: an approach to characterize fine-scale variation in fuels and fire in frequently burned longleaf pine forests. *International Journal of Wildland Fire* **18**, 315–325. doi:10.1071/WF08084

- Hudak A, Dickinson M, Bright B, Kremens R, Loudermilk L, O'Brien J, Hornsby B, Ottmar RD (2015) Measurements relating fire radiative energy density and surface fuel consumption – RxCADRE 2011 and 2012. *International Journal of Wildland Fire* **25**, 25–37. doi:10.1071/WF14159
- Johnson EA, Miyanishi K (2001) 'Forest fires: behavior and ecological effects.' (Academic Press: San Diego.)
- Johnston J, Wooster M, Lynham T (2014) Experimental confirmation of the MWIR and LWIR grey body assumption for vegetation fire flame emissivity. *International Journal of Wildland Fire* **23**, 463–479. doi:10.1071/WF12197
- Kennard DK, Outcalt KW, Jones D, O'Brien JJ (2005) Comparing techniques for estimating flame temperature of prescribed fires. *Fire Ecology* **1**, 75–84. doi:10.4996/FIRECOLOGY.0101075
- Kirkman LK, Goebel PC, Palik BJ, West LT (2004) Predicting plant species diversity in a longleaf pine landscape. *Ecoscience* **11**, 80–93.
- López A, Molina-Aiz FD, Valera DL, Peña A (2012) Determining the emissivity of the leaves of nine horticultural crops by means of infrared thermography. *Scientia Horticulturae* **137**, 49–58. doi:10.1016/J.SCIENTA.2012.01.022
- Loudermilk EL, Hiers JK, O'Brien JJ, Mitchell RJ, Singhanian A, Fernandez JC, Cropper WP, Jr, Slatton KC (2009) Ground-based LIDAR: a novel approach to quantify fine-scale fuelbed characteristics. *International Journal of Wildland Fire* **18**, 676–685. doi:10.1071/WF07138
- Loudermilk EL, O'Brien JJ, Mitchell RJ, Cropper WP, Hiers JK, Grunwald S, Grego J, Fernandez-Diaz JC (2012) Linking complex forest fuel structure and fire behaviour at fine scales. *International Journal of Wildland Fire* **21**, 882–893. doi:10.1071/WF10116
- Maldague X (2001) 'Theory and practice of infrared technology for nondestructive testing.' (Wiley: New York.)
- Meléndez J, Foronda A, Aranda JM, Lopez F, Lopez del Cerro FJ (2010) Infrared thermography of solid surfaces in a fire. *Measurement Science & Technology* **21**, 105504. doi:10.1088/0957-0233/21/10/105504
- Mitchell RJ, Hiers JK, O'Brien JJ, Jack S, Engstrom R (2006) Silviculture that sustains: the nexus between silviculture, frequent prescribed fire, and conservation of biodiversity in longleaf pine forests of the southeastern United States. *Canadian Journal of Forest Research* **36**, 2724–2736. doi:10.1139/X06-100
- Ottmar RD, Hiers JK, Butler BW, Clements CB, Dickinson MB, Hudak AT, O'Brien JJ, Potter BE, Rowell EM, Strand TM, Zajkowski TJ (2015a) Measurements, datasets and preliminary results from the RxCADRE project – 2008, 2011 and 2012. *International Journal of Wildland Fire* **25**, 1–9. doi:10.1071/WF14161
- Ottmar RD, Hudak AT, Prichard ST, Wright CS, Restaino JC, Kennedy MC, Vihnanek RE (2015b) Pre-fire and post-fire surface fuel and cover measurements collected in the southeastern United States for model evaluation and development – RxCADRE 2008, 2011 and 2012. *International Journal of Wildland Fire* **25**, 10–24. doi:10.1071/WF15092
- R Core Team (2013) 'R: a language and environment for statistical computing.' (R Foundation for Statistical Computing: Vienna.)
- Rogalski A, Chrzanowski K (2002) Infrared detection and devices. *Opto-Electronics Review* **10**, 111–136.
- Rowell EM, Seielstad CA, Ottmar RD (2015) Development and validation of fuel height models for terrestrial LiDAR – RxCADRE 2012. *International Journal of Wildland Fire* **25**, 38–47. doi:10.1071/WF14170
- Snyder WC, Wan Z, Zhang Y, Feng YZ (1998) Classification-based emissivity for land surface temperature measurement from space. *International Journal of Remote Sensing* **19**, 2753–2774. doi:10.1080/014311698214497
- Van Wagner C (1971) Two solitudes in forest fire research. Canadian Forest Service, Petawawa Forest Experiment Station, Information Report PS-X-29. (Chalk River, ON)
- Wiggers MS, Kirkman LK, Boyd RS, Hiers JK (2013) Fine-scale variation in surface fire environment and legume germination in the longleaf pine ecosystem. *Forest Ecology and Management* **310**, 54–63. doi:10.1016/J.FORECO.2013.07.030